6 DEVELOPEMENT OF A TESTBEAM TELESCOPE BASED ON MAPS

Contents

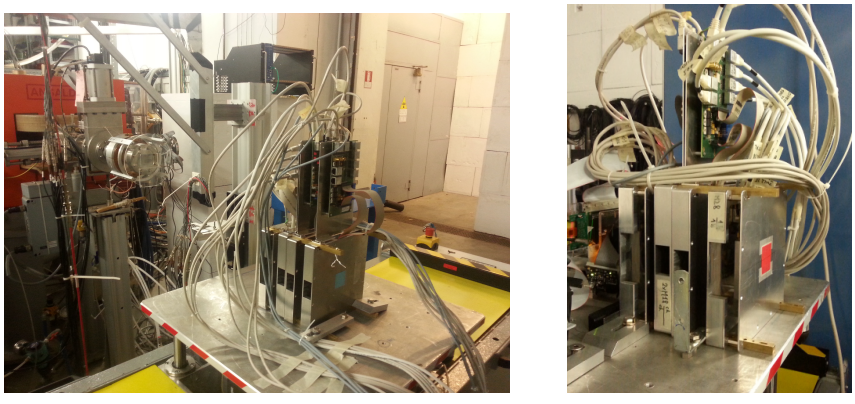

(a) Telescope overview

(b) Close up of the 7 layers composing the telescope

Figure 46: Telescope overview at the Beam Test Facility (INFN Laboratori Nazionali di Frascati)

A telescope composed of 4 planes of MIMOSA28 and 2 planes of MIMOSA18 chips (monolithic pixel sensors both developed in the 0.35 µm AMS process) is under development at the DAΦNE Beam Test Facility (BTF) at the INFN Laboratori Nazionali di Frascati (LNF)

in Italy. The telescope has been recently used to test a MIMOSA22ThrB chip (a monolithic pixel sensor built in the 0.18 µm TowerJazz process) and it is foreseen to perform tests on the full scale chips for the ALICE ITS upgrade in the early 2015. Fig. 46 shows the setup used during the testbeams of June and September 2014.

6.1 THE TELESCOPE SETUP

The telescope has been used so far in two testbeams at the BTF facility in Frascati (RM), the first in June and the second in September 2014.

In both the occasions the Device Under Test (DUT) was a MIMOSA22-ThrB but the telescope setup was slightly different.

6.1.1 June Setup

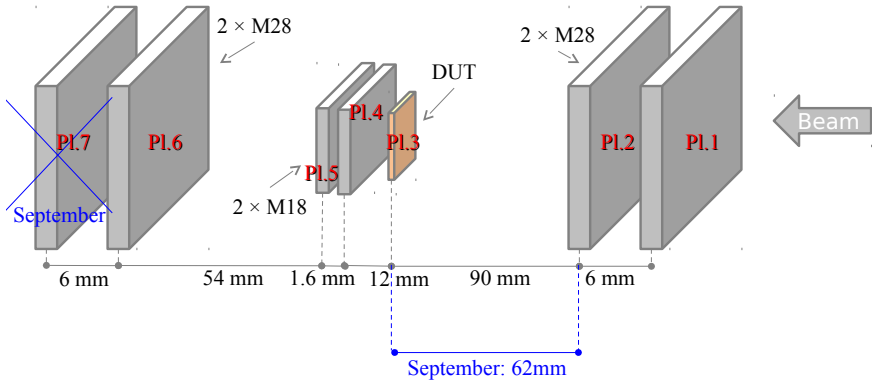

Figure 47: Telescope overview during testbeams (not to scale). In black the original setup used in June 2014, in blue the modifications made to the setup in September. In red the identification number of each plane is shown.

Fig. 47 shows a scheme of the telescope setup during the data taking. The incoming beam first hits the first pair of MIMOSA28 chips, placed at a distance of $\approx 0.6\,\mathrm{cm}$ from each other. The DUT (MIMOSA22ThrB) is placed at a distance of $\approx 9\,\mathrm{cm}$ from the second plane of MIMOSA28. A pair of MIMOSA18 is positioned very close (1.2 cm) to the DUT; the two sensors of MIMOSA18 are bonded on

the two opposite sides of the same board and are therefore very close to each other (1.6 mm), to minimize the effect of the lever arm for multiple scattering. A second pair of MIMOSA28 is placed downstream, whose first plane is placed at 5.4 cm from the MIMOSA18 doublet. Moreover between the first couple of MIMOSA28 and DUT a plane of MIMOSA22ThrA was placed. It was planned to be used as a further DUT but it was never connected with the DAQ. Anyway its presence must be taken into account for the multiple scattering effect.

During this testbeam we were not main users: the beam was not centred on the telescope and the particle rate was limited to a few particles/cm^2 per frame. As a consequence, the number of runs with very high statistics was limited.

6.1.2 September Setup

During the September testbeam the plane of MIMOSA22ThrA was removed from the telescope and the two first planes of MIMOSA28 were positioned closer to the DUT (at a distance of $\approx$ 6.2 cm). From the DUT going downstream no variations were made in the plane positions with respect to the June setup, nevertheless the seventh plane of the telescope (MIMOSA28) had some technical issues and was not included in the DAQ. Thus only 5 out of 6 planes of the telescope were available.

Profiting of being main users at the BTF, during this shift it was possible to center the telescope respect to the beam and to increase the particle rate up to $\approx$ 100 particles/cm^2 per frame.

Fig. 48 shows the beam profile as seen on the second MIMOSA28 plane: it is clearly visible the different position of the telescope with respect to the beam.

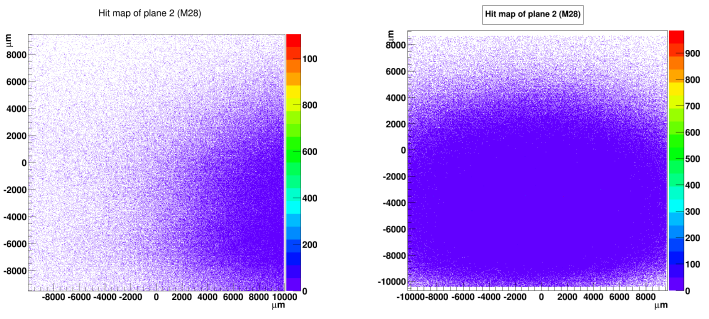

(a) June 2014 **(b)** September 2014

Figure 48: Profile of the beam as seen on one of the plane of MIMOSA28 in June (Fig. 48a) and in September (Fig. 48b)

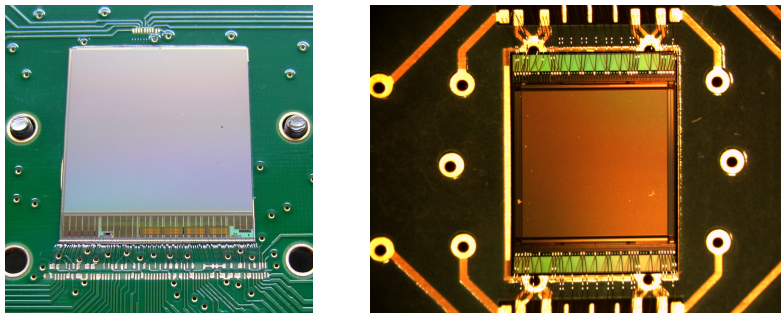

(a) MIMOSA28 (b) MIMOSA18

Figure 49: Close up of the MAPS sensors composing the telescope

6.1.3 MIMOSA28

The MIMOSA28 (see Fig. 49a) sensor (M28, ULTIMATE) is the final sensor developed for the upgrade of the inner layer of the vertex detector of the STAR experiment at RHIC. This chip has been fabricated in the 0.35 µm AMS opto process. It is a matrix of 928 (rows) × 960 (columns) digital pixels of 20.7 µm pitch, for a total chip size of $20.22 \times 22.71\,mm^2$. The sensor has an epitaxial layer thickness of 15 µm on a High Resistivity substrate (400 Ωcm) and has been thinned down to 50 µm to reduce the material budget. Pixel columns are readout in parallel, row by row; the readout time is 185.6 µs.

Each pixel includes an amplification and Correlated Double Sampling (CDS) and each end of columns is equipped with a discriminator. The threshold of the discriminator is programmable by JTAG slow control. After analog to digital conversion, the digital signals pass through the zero suppression block: digital signals are processed in parallel on 15 banks, then arranged and stored in a memory row by row.

6.1.4 MIMOSA18

The Mimosa-18 sensor (M18) [68] has been fabricated in the 0.35 µm AMS opto process and is a composed of 4 matrices of 256 × 256 analog pixels with a pitch of 10 µm. Therefore a single sensor consists of an array of 512 × 512 pixels, providing a total area of $5 \times 5\,mm^2$.

The sensor is fabricated using a standard 14 µm thick epitaxial layer and has been thinned down to 50 µm. A simple read out architecture is used: it consists of a 2-transistor pixel cell (half of a source follower plus a readout selection switch) connected to the charge collecting Nwell diode, continuously biased by another diode (forward biased) implemented inside sensing Nwell. The size of the sensing Nwell diode is of 4.4 µm × 3.4 µm. The signal information from each pixel is serialized by a circuit (one per sub-array), which can withstand up to

a 25 MHz readout clock frequency. However, all the results presented in this work were obtained with a 20 MHz clock, which provides a full frame readout time of ~ 3 ms.

In this architecture, the frame readout time is equal to the signal integration window. Information from two consecutive frames was read out, one frame before and one frame after each trigger. Correlated double sampling (CDS) method was used for hit reconstruction.

6.1.5 MIMOSA22 ThrB

The MIMOSA22-ThrB (M22-ThrB) [69] has been designed in TowerJazz 0.18 µm process on a high resistivity epitaxial layer. The sensor is composed of a matrix of 64×64 elongated pixels, with a pixel size of $33\mu m \times 22\mu m$. Its architecture is based on the MIMOSA22 which is a fast binary readout MAPS, with an integration time of 6.4 µs. At the bottom of the matrix there are 56 columns composed of two discriminators for double row readout and 8 columns formed of 2 output buffers for double row readout. The matrix is controlled by internal fully programmable digital sequencer and integrates each one output multiplexers for 16 binary outputs. The chip is driven by a 100 MHz clock. The setup with programmable registers is accessed via an embedded slow control JTAG interface.

6.1.6 Data acquisition system

The Data Acquisition system (DAQ) is based on the VME bus standard. The whole system consists of four V1495 (General Purpose VME board, equipped with a EP1C20 Altera Cyclone FPGA) modules by Caen, one ADC SIS3300 and one ADC SIS3301 boards by Struck, one V895 (16 channel leading edge discriminator) by Caen and one V2718 VME controller optical bridge by Caen. The 8 analog signals from the M18 are sampled by the 8 differential inputs of the SIS3301 module. The SIS3300 has 8 single-ended analog inputs, which are used to acquire the data from the beamline calorimeter and the beam signal from the BTF. This BTF signal has a repetition rate of 25 ns (the pulse duration is a few ns) and is used as trigger for the whole system. The trigger signal is sent to one input of the V895 board (low threshold discriminator), which in its turn sends its output pattern to one of the V1495, which also acts as Trigger Supervisor. The Trigger Supervisor sends the trigger signals to all the other V1495 modules; it also manages the BUSY signal: at each trigger, the Trigger Supervisor stops and, before accepting more trigger signals, it waits to be reset by the acquisition software. The Trigger Supervisor also produces a common clock at 80 MHz which is distributed to all the four V1495. One of the four V1495 is then used to generate the control signals for the SIS3300 and SIS3301, which are working at a clock frequency

of 20 MHz (the same frequency as the M18); the other V1495 modules are used to generate all the digital control signals for the 7 chips, to readout and store in some FIFOs internal to the FPGA the digital outputs from the four M28 and the two M18. The initialization procedures for the four M28 and the two M18 are managed by a software which reads out the respectively ASCII Configuration Files and sends the proper signals to the sensors through the V1495, which act as a parallel port.

6.2 ANALYSIS PROCEDURE

An electron beam with an energy of 500 MeV has been used. Data were collected for different threshold values in Signal to Noise ratio (SNR) applied to the DUT in order to test the dependence of the efficiency on the SNR cut.

Data were analysed using TAF [70], which stands for TAPI Analysis Framework, the package created and managed by the PICSEL group at IPHC (Strasbourg, France) to characterize CMOS pixel and strip sensors from data acquired with various sources (X-rays, β-rays, laser) or with particle beams.

The cluster position is reconstructed as centre of gravity of the pixels belonging to the cluster.

6.2.1 Alignment

Fig. 50 shows the correlation plots in horizontal and vertical direction between the two planes of MIMOSA18. The plots are built plotting the horizontal (vertical) hit position on one plane as a function of all the other horizontal (vertical) hit positions of the same event on the other plane. If a particle has crossed the telescope the hit position on the two planes are necessarly correlated.This leads to a region in the scatter plot where a correlation between the hit positions in the two planes is clearly visible

The different correlation directions in the scatter plot along the two coordinates are due to the mutual position of the two MIMOSA18 sensors; indeed, they are mounted on the two side of the same board rotated of 180° one respect to the other.

The correlations between hits of different planes mean that particles have crossed the telescope, but to properly track through all the planes it is necessary to apply some corrections to the measured plane positions in order to take into account their real mutual position.

The 6 planes of the telescope were first aligned plane by plane (alignment is not done globally), starting from one plane chosen as reference (called *seed plane*) with an iterative semi-automatic procedure. The track starts with a single hit in the reference plane and

with zero slope. Then, the track seed extrapolation to the next plane defines the centre of a circular search area. If there are hits on this plane within the search area, the nearest one to the centre is associated to the track. The track parameters are then recomputed and the iteration goes on with the next plane. Once all the planes have been scanned, the track is tested against selection cuts.

Due to the different conditions during the two testbeams, align procedure has been performed in different way with the June and September data.

In June the alignment strategy started with the definition of plane 6 as the reference plane. Then plane 7 was aligned with respect to plane 6. Using tracks passing through plane 6 and 7, plane 4 and 5 were then aligned. Finally tracking with plane 4, 5, 6 and 7 the alignment has been performed on plane 1 and 2. DUT was then aligned with respect to the telescope.

In September it was not possible to use the same procedure since plane 7 was not included in the DAQ. Thus in the alignment procedure plane 2 was considered as the reference plane, then plane 1 was aligned with respect to that. Profiting of the high statistics, the DUT was included in the procedure and aligned with respect to plane 1 and 2. Then planes 4 and 5 were aligned using as a reference the first three planes and, eventually, plane 6 was aligned with respect to the other five planes.

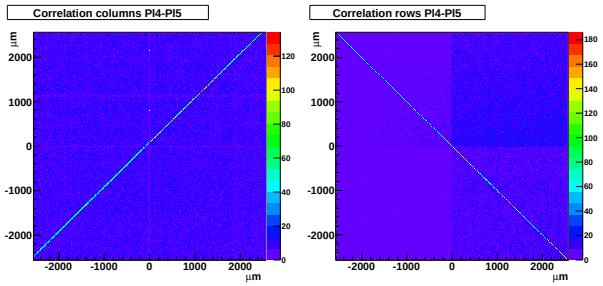

Figure 50: Correlation plots between hits on Plane 4 and 5 (M18) of the Telescope (September setup). Left panel: correlation of hits along column direction. Right panel: correlations of hits along rows direction.

6.2.2 Tracking

After alignment, tracks reconstruction has been performed. As for the tracking strategy, a hit in at least 4 out of 6 planes (4 out of 5 for September data) is required to make a track. Usually a distance lower than 400 µm is required for a hit-track association. The track fitting model is a straight line (parameters obtained from a least square fit): no multiple scattering is considered. The DUT is, of course, excluded from the tracking procedure.

Fig. 51 shows the statistics on the tracking results. The left panel (Fig. 51a) represents the distribution of the fraction of times (in percentage) each plane has been used to fit a track while the right one shows the distribution of the number of hits on different planes used to fit a track. It is possible to notice that in June nearly 100% of the tracks has been obtained with 4 planes, the majority using plane number 1,2,6 and 7 (i.e. the four plane of M28, composing the telescope). This is due to the fact that having 4 planes of M28, which have a sensitive area $\approx$ 16 times greater than the M18, and requiring at least 4 points to make a track, excludes from the tracking algorithm the M18 sensors in most of the cases. In the analysis of September data, instead, the majority of tracks has been obtained using 5 planes, all the telescope planes available. The reason is that in this case requiring 4 hits to make a track necessarily includes one of the M18 planes in the fit procedure and, since they are so close one to the other, almost always it is possible to find a hit associated to the track within the searching region on the other M18 plane (much less affected by multiple scattering effect).

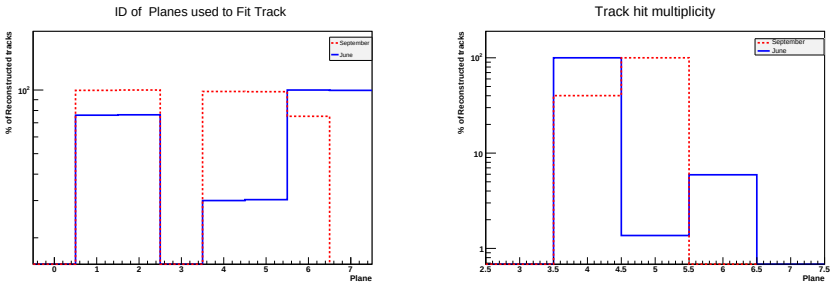

(a) Distribution of the fraction of times each plane has been used to fit a track.

(b) Distribution of the number of planes used to fit a track.

Figure 51: Statistics on the planes used (Fig. 51a) and on the number of hits on different planes (Fig. 51b) used to fit a track. Blue solid distributions refer to June data, while red dotted ones refer to September data.

Fig. 52 shows the residuals distributions for the different telescope planes in the vertical coordinate after the tracking procedure. They are obtained as the distribution of the hit-track distance in the vertical direction. Similar results have been obtained in the other coordinate. Plots are normalized to the number of reconstructed tracks. This plots can be used to check the alignment precision reached. The residuals distribution should have a gaussian shape, centred at 0. Their width depends on the resolution of sensor itself, the global resolution of the telescope and on the multiple scattering effect.

From the distributions, the different conditions and strategy used to align the telescope in the two testbeams are evident.

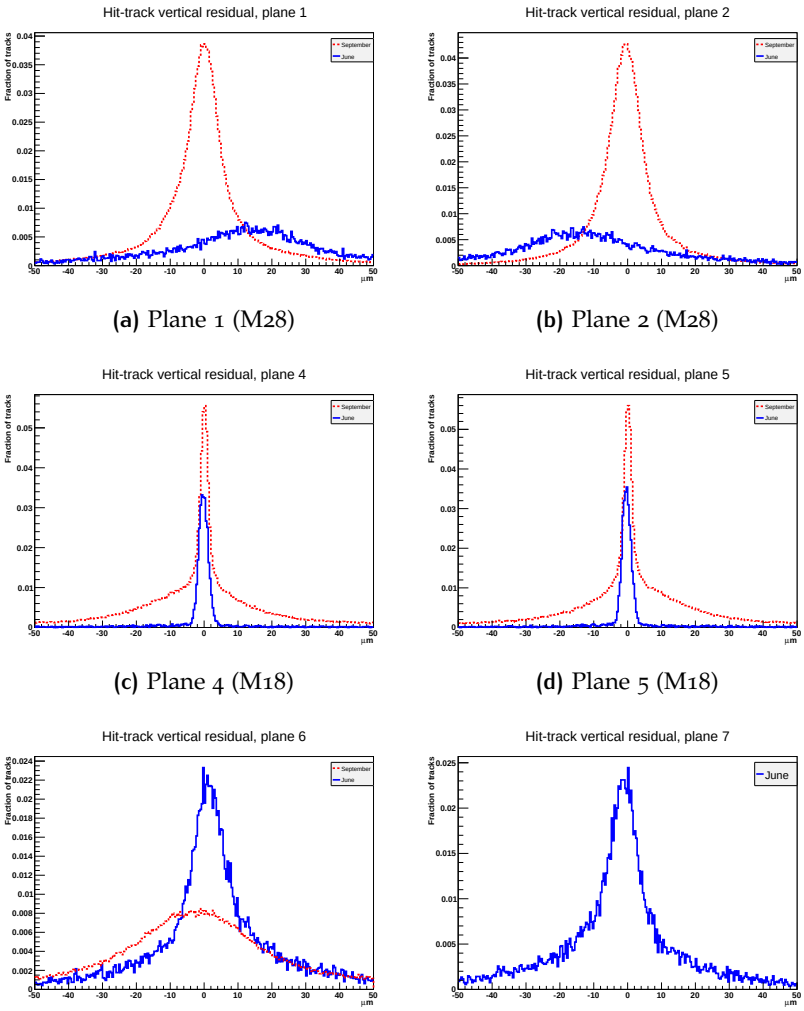

(a) Plane 1 (M28)

(b) Plane 2 (M28)

(c) Plane 4 (M18)

(d) Plane 5 (M18)

(e) Plane 6 (M28)

(f) Plane 7 (M28)

Figure 52: Telescope planes residual (hit-track distance) distributions in vertical direction after alignment procedure. Distributions are normalized to the total number of reconstructed tracks. Blue solid distributions refer to June data, while red dotted ones refer to September data.

As far as June is concerned, the alignment strategy started from plane 6 and the first couple of planes that were aligned was 6 and 7, while the last was 1 and 2. For this reason it is possible to notice that the residuals distributions of the last two planes of the telescope show a narrow peak 0-centred (with a FWHM of $\approx 10\,\mu m$) while the residuals of the first two planes have a broad distribution which is not centred at 0 but rather at $\approx 15\,\mu m$ for plane 1 and at $\approx -15\,\mu m$ for plane 2. This means that they are not perfectly aligned with respect to the others planes and that the multiple scattering effect has an important effect on the tracking precision.

The different strategy applied in September led to an opposite situation in the residuals distribution, in this case in fact the narrow distributions are on plane 1 and 2 while, although centred at 0, plane 6 presents a broad peak. This means that the higher statistics and the better position with respect to the beam in this occasion improved the alignment capability of the telescope but the multiple scattering still has an important effect.

In the case of plane 4 and 5, instead, the small pitch of the pixel, the analogue readout and their close mutual position allow to have a distance of the tracks associated to a hit on the DUT distribution whose width is comparable for the two testbeams.

6.3 ANALYSIS RESULTS

6.3.1 Efficiency

The detection efficiency of the DUT has been measured for different values of the discriminators threshold set on the DUT quoted in units of noise (in the following noted as *SNR threshold* applied, quoted in terms of number of σ). Efficiency has been evaluated as the ratio between the number of tracks associated to a hit in the DUT, within a certain distance, and the total number of tracks passing through the sensitive region of DUT. As a further selection criteria a cut on χ^2 has been applied. Only tracks with $\chi^2 < 45$ have been accepted.

Fig. 53 shows the map of the hits on the DUT associated to a track (left panels) and the map of the track impact positions on the DUT which could not be associated with any hit on the DUT (right panels). Two runs with the same SNR threshold applied on the DUT (9 σ) are compared: in the top panels plots refer to June data, in the bottom to September ones.

From the plots it is evident the different statistics available in the two runs (see Tab. 9). However in both the testbeams the whole area of the DUT was illuminated by the sensors and no zone of inhomogeneity in the rejection of the tracks are present, meaning that the behaviour of the DUT is the same over the whole sensitive area.

Fig. 54 shows, for the same runs previously discussed, the distribution of the track-hit distance of the tracks associated to an hit on the DUT. The majority of the hits has a distance to the associated track below 100 μm. In this case the maximum distance allowed to match hit with tracks was set to 500 μm in order to take into account the possible great effect of multiple scattering for electrons of 500 MeV. The cut seems reasonable since it seems to cut only the very tail of the distributions.

Fig. 55 shows the efficiency as a function of the SNR threshold applied to the discriminators of the DUT. For the June data the calcula-

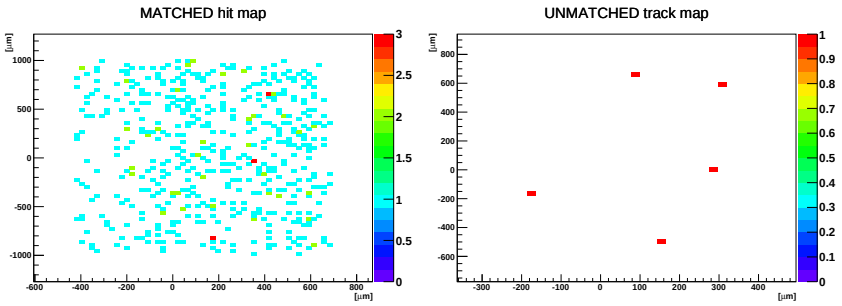

(a) June **(b)** June

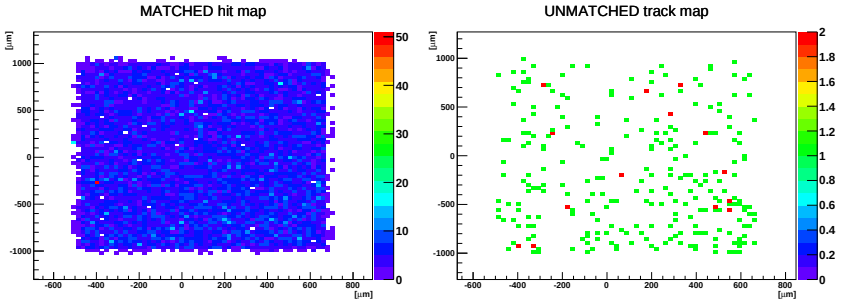

(c) September **(d)** September

Figure 53: Left panels: maps of hits (Cluster Centre of Gravity) on the DUT matched to a track crossing the DUT. Right panels: maps of track impact positions on the DUT which could not be associated to any tracks in the DUT. Top plots refer to June data, bottom to September ones. Both in June and September the SNR threshold on the DUT was 9σ and the maximum distance to associate hit to tracks was 500 µm.

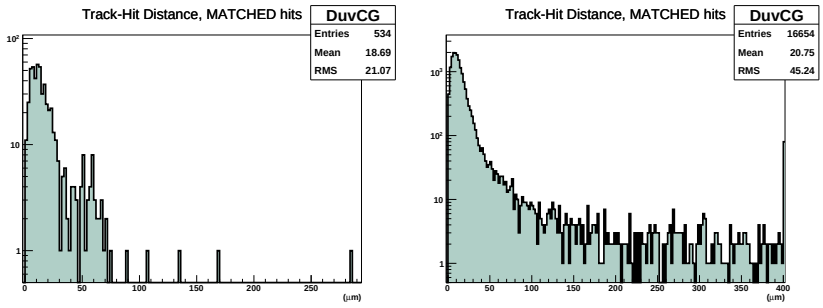

(a) June **(b)** September

Figure 54: Distribution of the track-hit distance of hits matched to a track on the DUT in a run where the SNR threshold on the DUT was 9σ.

tion has been made considering both the whole area of the DUT and the area excluding a 2-pixels external crown, in order to exclude uncompleted clusters. The maximum distance to associate hit to tracks on DUT was 500 µm. In September instead two different cuts on the

maximum distance have been used: 400 µm and 500 µm; in both cases the 2-pixels external crown has been removed from the region of interest for the hits on the DUT. The numerical values of the efficiencies shown in Fig. 55 are reported in Tab. 9. Errors on the efficiency have been evaluated as the variance of a binomial distribution.

It is possible to notice that:

- Excluding the two pixel external crowns has a marginal effect, efficiency evaluated with or without this region are compatible within the error bars. It has been chosen to exclude the external region in the second testbeam in order to avoid cut clusters.
- The different maximum distances affect the efficiency evaluation especially at higher SNR threshold.
- Both in June and in September data efficiency is close to 99% up to SNR threshold of 9σ and then it drops, meaning that for cuts $> 9\,\sigma$ we are starting to lose signal.
- Even though the maximum distance allowed to associate hit to track was 500 µm, actually, the hit-to-track distributions (Fig. 54) show that the association is mostly made within 100 µm. With a fake hit rate at this SNR of $3 \cdot 10^{-4}$ (see Sec. 6.3.3) the possible contribution from noisy pixels within the searching region is negligible.
- June and September evaluations of the efficiencies for runs with the same thresholds are compatible within the errors.

6.3.2 Spatial Resolution

Spatial resolution has been evaluated with the June and September data using a 9σ SNR threshold.

The spatial resolution of the DUT has been estimated from the hits residual distributions. These distributions are obtained with the difference between the impact position of the particle extrapolated from the track direction and the position of the hit associated to that track on the DUT. The hit position on the DUT is evaluated as the centre of gravity of the cluster distribution.

Fig. 56 shows, as example, the residual distributions on the DUT in both vertical and horizontal directions for the September dataset. Similar results have been obtained in June. The distributions are gaussian shaped and centred at 0. Starting from the width of the residuals distribution (evaluated as the standard deviation of a gaussian fit) it is possible to give an estimation of the spacial resolution of the DUT.

The width of the residual distribution, however, is not only affected by the DUT resolution but also by the resolution of the telescope itself.

	June $d_{hit-tr} < 500\,\mu m$			September $d_{hit-tr} < 400\,\mu m$			September $d_{hit-tr} < 500\,\mu m$		
σ	Associated tracks	Tot. tracks through DUT	Efficiency [%]	Associated tracks	Tot. tracks through DUT	Efficiency [%]	Associated tracks	Tot. tracks through DUT	Efficiency [%]
6				$47228 \pm 0.5\%$	$47257 \pm 0.5\%$	99.96 ± 0.02	$42247 \pm 0.5\%$	$47257 \pm 0.5\%$	99.900 ± 0.008
7	$309 \pm 5\%$	$311 \pm 5\%$	**99.2 ± 0.5**	$159754 \pm 0.2\%$	$160223 \pm 0.2\%$	99.71 ± 0.01	$159939 \pm 0.3\%$	$160223 \pm 0.2\%$	**99.82 ± 0.01**
8	$1778 \pm 2\%$	$1790 \pm 2\%$	**99.3 ± 0.2**	$78763 \pm 0.4\%$	$79332 \pm 0.3\%$	99.28 ± 0.03	$78910 \pm 0.4\%$	$79332 \pm 0.4\%$	**99.47 ± 0.03**
9	$631 \pm 4\%$	$640 \pm 4\%$	**99.1 ± 0.4**	$169884 \pm 0.2\%$	$172601 \pm 0.2\%$	98.42 ± 0.03	$170405 \pm 0.2\%$	$172601 \pm 0.2\%$	**98.72 ± 0.03**
10	$829 \pm 3\%$	$864 \pm 3\%$	**96.0 ± 0.7**	$99508 \pm 0.3\%$	$102962 \pm 0.3\%$	96.64 ± 0.06	$99848 \pm 0.3\%$	$102962 \pm 0.3\%$	**96.97 ± 0.05**
11	$3677 \pm 1\%$	$3917 \pm 1\%$	**93.9 ± 0.4**	$79226 \pm 0.4\%$	$84491 \pm 0.3\%$	93.77 ± 0.09	$11771 \pm 0.4\%$	$12485 \pm 0.3\%$	**94.32 ± 0.08**
13				$8094 \pm 1\%$	$9059 \pm 1\%$	89.3 ± 0.3	$8164 \pm 1\%$	$9059 \pm 1\%$	90.1 ± 0.3
14				$7724 \pm 1\%$	$8982 \pm 1\%$	86.0 ± 0.4	$7810 \pm 1\%$	$8982 \pm 1\%$	86.9 ± 0.3
15				$21114 \pm 0.7\%$	$25058 \pm 0.6\%$	84.4 ± 0.2	$21595 \pm 0.7\%$	$25058 \pm 0.6\%$	86.2 ± 0.2
16				$34135 \pm 0.5\%$	$41771 \pm 0.5\%$	81.7 ± 0.2	$79699 \pm 0.5\%$	$84491 \pm 0.3\%$	84.3 ± 0.2

Table 9: Summary of the efficiency values found for different SNR used to acquire the DUT data (σ) and number of tracks used to evaluate the efficiencies. In bold font values obtained in the same conditions in June and September.

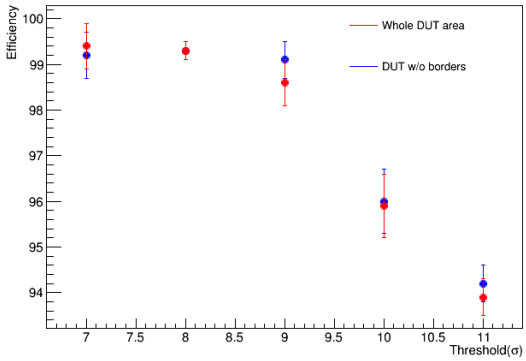

(a) June dataset. Blue points are obtained excluding the two external pixels crown of the DUT matrix, red ones considering instead the whole DUT matrix. Maximum distance to associate hits to tracks on the DUT is 500 µm

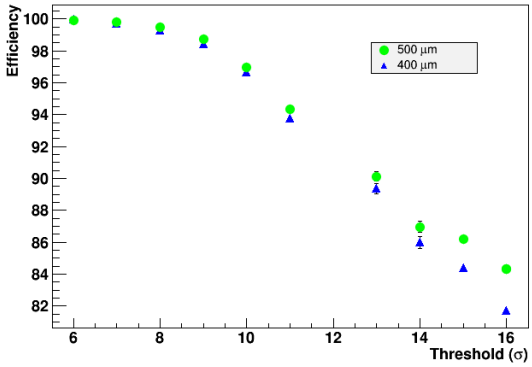

(b) September dataset. Green circles are obtained considering as maximum distance to associate hits to tracks on the DUT 500 µm, blue triangles using instead 400 µm. In both cases the external two pixels crown of the DUT has been excluded from the searching region.

Figure 55: DUT Efficiency as a function of the SNR cut used to acquire the DUT data

	Horizontal [µm]	Vertical [µm]
June	9.1 ± 0.5	10.7 ± 0.4
September	8.65 ± 0.02	10.59 ± 0.02

Table 10: DUT Residual width (σ of the gaussian fit of distributions shown in Fig. 56) in a run with 9σ threshold

Namely the residual distribution is a convolution of two gaussians with different width: one including the contribution of the telescope resolution and the multiple scattering effect (with a standard devi-

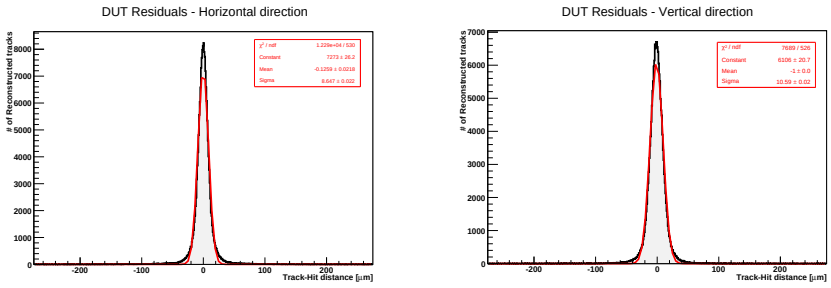

(a) DUT residuals distribution, columns direction

(b) DUT residuals distribution, rows direction

Figure 56: DUT residuals distributions along columns (Fig. 56a) and rows (Fig. 56b) directions. The hit position on the DUT is reconstructed as the center of gravity of the cluster. September setup configuration. SNR cut on DUT data was 9 σ

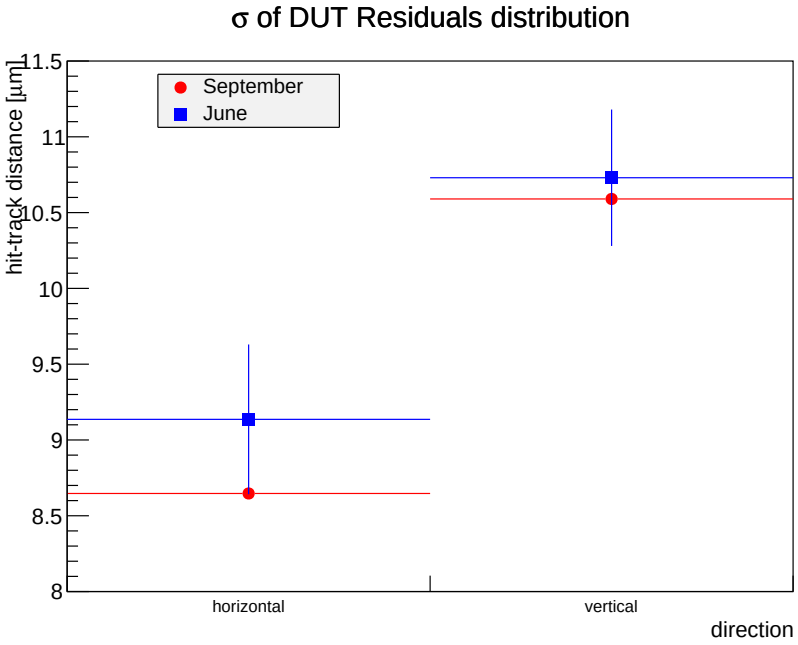

Figure 57: Comparision of the residual distribution width (evaluate obtained in June and in September

ation noted as res_{TEL}) and one due to the DUT resolution (with a different width res_{DUT}). For this reason, the σ of the residual distribution can be expressed like shown in Eq 21.

$$\sigma = \sqrt{res_{tel}^2 + res_{DUT}^2} \tag{21}$$

Fig. 57 shows a comparision of the σ (standard deviation of the gaussian fit) of the residuals distribution for both June and September data. It is possible to notice that the two results obtained are compatible within the errors, which, in this case, are expressing only the

statistical uncertainty of the interpolation. However this uncertainty for the September data is much more smaller thanks to the higher statistics available. The same results are summarized also in Tab. 10. The differences between the horizontal and vertical directions can be explained with the different pitch of the pixels in the two directions (22 μm in the horizontal direction and 33μm in the vertical one).

A first estimation for the telescope resolution has been obtained with a Toy Monte-Carlo included in the TAF software package, implementing the geometry used for the testbeam, obtaining the same results for the two configurations:

$$res_{tel} = (8.0 \pm 0.5)\ \mu m \tag{22}$$

This led to the estimated DUT spatial resolution noted in tab. 11

	DUT resolution	
	Horizontal [μm]	Vertical [μm]
June	4.3 ± 0.7	7.1 ± 0.6
September	3.3 ± 0.5	6.9 ± 0.6

Table 11: DUT Resolution estimation. The SNR threshold set on DUT discriminators was 9σ. Only statistical uncertainty are quoted.

The results obtained are generally in line with the ITS upgrade requirement, however a few approximations were done:

- As far as June setup is concerned, the plane of M22ThrA, which should be considered as a passive plane, was not included in the simulation. The Toy Monte-Carlo indeed has not this possibility currently implemented.
- The uncertainties here quoted only include the statistical error deriving from the fit and the simulation. They do not take into account a possible systematic effect due to inefficiencies in the alignment procedure. In particular the TAF alignment procedure has been developed for much higher energy of the incoming beam where multiple scattering has a smaller effect.

To overcome this limitations some GEANT3 simulations are currently ongoing to better estimate the telescope resolution. The idea of this simulations is to use GEANT3 to implement the geometry of the telescope and to transport particles through the telescope and then use directly TAF to reconstruct the tracks. In this way the DUT residuals distribution obtained are taking into account only the contribution of the multiple scattering since the impact position on the DUT is known in the simulation.

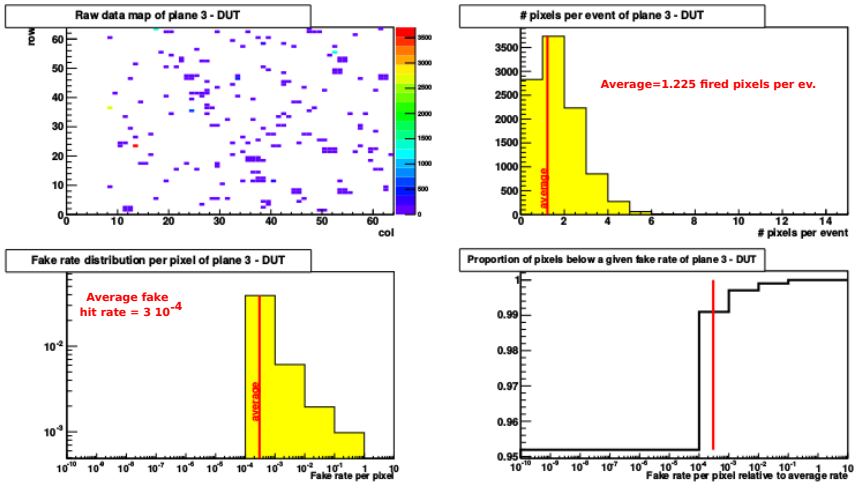

Figure 58: Top left panel: raw hit distribution in a run of 1000 events without beam with a SNR threshold of 9σ . Top right panel: distribution of the number of hit pixels in each event during the run. Average number of hit pixels corresponding to 1.225 is indicated in the plot . Bottom left panel: fake hit rate ditribution obtained as the frequency of hit per pixel per event. Bottom right panel: distribution of the fraction of pixels below a certain fake hit rate value.

Another option under investigation is to directly measure the telescope resolution by keeping the very same geometry for the telescope planes, and replacing the DUT with a high resolution device. The M18 would be a proper candidate: it is an analog detector with a very small pitch (10 µm), which might provide a resolution close to 1 µm. We plan to carry out this measurement in one of the next test beams.

6.3.3 Fake Hit Rate

Fake hit rate has been evaluated in events with no beam, for different thresholds set on the DUT discriminators.

Fig. 58 shows the results obtained for SNR threshold on DUT equal to 9σ. Top left plot is showing the hit map on the DUT over 1000 events, the top right one presents the distribution of the number of fired pixels per events, the average of the distribution is also plotted and, in this case, was equal to 1.225 fired pixels per event. *Fake hit rate* is evaluated dividing the number of fired pixels per events by the total number of pixels in the matrix and the number of events. The left bottom plot of Fig. 58 shows the fake hit rate distribution. The average fake hit rate per pixel is $3\,10^{-4}$. The right bottom plot shows the fraction of pixels in the sensor which have a fake hit rate lower than a certain value. It is possible to see that the 99% of pixels in the DUT has a fake hit rate below 10^{-3}.

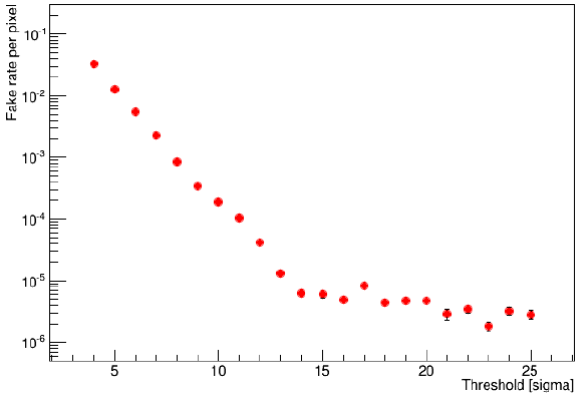

Figure 59: Fake hit rate on the DUT as a function of the SNR cut applied on the DUT data taking

Calculation has been repeated for different SNR thresholds and the average Fake Hit Pixel as a function of the threshold applied is shown in Fig. 59.

It is possible to notice that the fake hit rate decreases up to $SNR_{thr} = 13\,\sigma$ and then remains stable to a value $\approx 10^{-5}$/pixel.

Although this result is in line with the requirements for the upgrade it has to be mentioned that the prototype used as DUT has a small number of pixels and it is not corrected for the known effect of "Random Telegraph Signal" noise (RTS). The RTS noise originates from the presence of defects in the oxide layer of a MOS transistor. It depends on different variables including temperature, gate voltage of the transistor and the oxide thickness. It manifests itself as discrete changes of individual pixel output between two (or more) levels. While the amplitude of this signal is well defined, its period is random and may reach minutes. The amplitude of the RTS is sufficient to exceed the pre-set threshold of the detector and may therefore generate fake hits. The Fake Rate here described is dominated by these two effects.

7 CONCLUSION

Recent developments in the field of Monolithic Active Pixel Sensor (MAPS) technology have opened a window of possibilities for their use as vertexing and tracking detectors in particle physics experiments. ALICE has an elaborate upgrade programme based on the upgrade of the LHC in 2018-19 during the second Long Shutdown (LS2).

ALICE has already demonstrated very good capabilities for the study of heavy ion collisions at high energy in its first three years of operation. But there are particular measurements, like high precision measurements of rare probes over a wide range of momenta, which would require high statistics and are not satisfactory or even possible with the present experimental setup. These measurements would help to achieve the long term physics goals of ALICE and would go a long way forward in understanding and characterizing the Quark Gluon Plasma (QGP) state of matter. The LHC upgrade features which primarily motivated the ALICE upgrade programme are Pb–Pb collisions with a high interaction rate of up to 50 kHz, corresponding to an instantaneous luminosity $\mathcal{L} = 6 \times 10^{27} \mathrm{cm}^{-2}\mathrm{s}^{-1}$ and, the installation of a narrower beam pipe.

Accordingly, ALICE would require detector upgrades to cope with the new scenario.In particular the upgraded ALICE apparatus should improve tracking and vertexing capabilities, radiation hardness and should allow readout of all interactions to accumulate enough statistics for the extended physics programme. The objective is to accumulate $10\,\mathrm{nb}^{-1}$ of Pb-Pb collisions, recording about 10^{11} interactions.

Within this upgrade strategy, the Inner Tracking System (ITS) upgrade forms an important cornerstone, providing improved vertexing and readout capabilities. The new ITS will have a barrel geometry consisting of seven layers of Monolithic Active Pixel Sensors (MAPS) with high granularity. The geometry is optimized for high efficiency, both in standalone tracking and ITS-TPC combined tracking.

TowerJazz 0.18 µm technology has been selected for designing the pixels for ITS upgrade. This technology provides attractive features like, for example, the option to implement a deep p-well allowing the implementation of a full CMOS process in the pixel.

Several prototypes have been designed to investigate and validate the different design strategies and the different components of the pixel detector using this technology. The design R&D is being carried out at CNU (Wuhan, China), CERN, INFN (Italy), NIKHEF (The Netherlands), Yonsei (South Korea) and IPHC Strassbourg.

The ongoing research and development on these pixels investigates different design strategies and would converge towards at the beginning of 2015.

MIMOSA32 and MIMOSA32Ter, developed at IPHC Strassbourg, were one of the first prototypes designed with the TowerJazz technology for the upgrade program. The motivation was to validate the technology in terms of charge collection and radiation tolerance. These prototypes also implemented deep p-well structures (without implementing a full CMOS in the pixel circuit) to qualify its usage for future prototypes using a full CMOS process.

This thesis studied the results of tests and characterization of pixel structures of these prototypes and concluded that the technology provided the basic requirements of charge collection and radiation tolerance. It also concluded that the addition of a deep p-well maintains satisfactory performance even after irradiation. This marks a starting point for future prototypes where the deep p-well could be implemented in a full CMOS process, thus allowing in-pixel sophisticated signal processing circuits.

To study the detection efficiency and the spacial resolution of the prototypes a telescope of sensors capable to provide external tracking is needed. In this thesis the development of a telescope of MAPS sensor carried out at the LNF Laboratory in Frascati is presented. It is composed of six planes of MAPS sensors: 4 planes of MIMOSA28 (0.35 μm AMS opto process, 928 rows $\times$ 960 columns, pitch of 20.7 μm, binary readout) and two of MIMOSA18 (0.35 μmAMS opto process, 4 matrices of 256 $\times$ 256 pixels, pitch of 10 μm, analog readout). The incoming beam first goes through two planes of MIMOSA 28, then the DUT is placed followed by two planes of MIMOSA18 and another couple of MIMOSA28.

This thesis shows the results obtained with this telescope using the MIMOSA22-ThrB as DUT protoype in two testbeams carried out in June and September 2014. Detection efficiency, spatial resolution and fake hit rate of this prototype have been evaluated during these two testbeams and all the measured parameters are in line with the requirements set by the ITS upgrade.

This thesis validated the telescope setup which will be used for a comparative study of the two full scale protoypes designed for the ALICE upgrade: the FSBB developed in Strasbourg by IPHC PICSEL group and ALPIDEfs developed by the collaboration of CNU (Wuhan, China), CERN, INFN (Italy), NIKHEF (The Netherlands), Yonsei (South Korea). First test on the full scale prototypes are foreseen either for the end of 2014 or for the beginning of 2015.

BIBLIOGRAPHY

[1] Edward V. Shuryak. "Quantum chromodynamics and the theory of superdense matter". In: *Physics Reports* 61.2 (1980), pp. 71–158. ISSN: 0370-1573. DOI: http://dx.doi.org/10.1016/0370-1573(80)90105-2. URL: http://www.sciencedirect.com/science/article/pii/0370157380901052 (cit. on p. 3).

[2] Frithjof Karsch. "Lattice results on QCD thermodynamics". In: *Nucl.Phys.* A698 (2002), pp. 199–208. DOI: 10.1016/S0375-9474(01)01365-3. arXiv: hep-ph/0103314 [hep-ph] (cit. on p. 3).

[3] O.W. Greenberg and C.A. Nelson. "Color models of hadrons". In: *Physics Reports* 32.2 (1977), pp. 69–121. ISSN: 0370-1573. DOI: http://dx.doi.org/10.1016/0370-1573(77)90035-7. URL: http://www.sciencedirect.com/science/article/pii/0370157377900357 (cit. on p. 4).

[4] Antonio Pich. "Aspects of quantum chromodynamics". In: (1999). arXiv: hep-ph/0001118 (cit. on p. 4).

[5] M. E. Peskin and D. V. Schroeder. *An Introduction to Quantum Field Theory*. Reading: Addison-Wesley, 1995 (cit. on p. 5).

[6] Michael J. Fromerth and Johann Rafelski. "Hadronization of the quark universe". In: (2002). arXiv: astro-ph/0211346 (cit. on p. 5).

[7] Frithjof Karsch. "Properties of the Quark Gluon Plasma: A lattice perspective". In: *Nucl. Phys.* A783 (2007), pp. 13–22. DOI: 10.1016/j.nuclphysa.2006.11.035. arXiv: hep-ph/0610024 (cit. on p. 6).

[8] A. Chodos et al. "New extended model of hadrons". In: *Phys. Rev. D* 9 (12 June 1974), pp. 3471–3495. DOI: 10.1103/PhysRevD.9.3471. URL: http://link.aps.org/doi/10.1103/PhysRevD.9.3471 (cit. on p. 7).

[9] Tetsuo Hatsuda and Teiji Kunihiro. "QCD phenomenology based on a chiral effective Lagrangian". In: *Physics Reports* 247.5-6 (1994), pp. 221–367. ISSN: 0370-1573. DOI: 10.1016/0370-1573(94)90022-1. URL: http://www.sciencedirect.com/science/article/pii/0370157394900221 (cit. on p. 7).

[10] Prashant Shukla. "Glauber model for heavy ion collisions from low energies to high energies". In: (2001). arXiv: nucl-th/0112039 (cit. on p. 8).

[11] Cheuk-Yin Wong. *Introduction to high-energy heavy ions collision*. World Scientific, 1994 (cit. on pp. 9, 11).

[12] ALICE Collaboration. "Centrality Dependence of the Charged-Particle Multiplicity Density at Midrapidity in Pb-Pb Collisions at $\sqrt{s_{NN}} = 2.76$ TeV". In: *Phys. Rev. Lett.* 106 (3 Jan. 2011), p. 032301. DOI: 10.1103/PhysRevLett.106.032301. URL: http://link.aps.org/doi/10.1103/PhysRevLett.106.032301 (cit. on p. 11).

[13] ALICE Collaboration. "Charged-Particle Multiplicity Density at Midrapidity in Central Pb-Pb Collisions at $\sqrt{s_{NN}} = 2.76$ TeV". In: *Phys. Rev. Lett.* 105 (25 Dec. 2010), p. 252301. DOI: 10.1103/PhysRevLett.105.252301. URL: http://link.aps.org/doi/10.1103/PhysRevLett.105.252301 (cit. on p. 11).

[14] Serguei Chatrchyan et al. "Dependence on pseudorapidity and centrality of charged hadron production in PbPb collisions at a nucleon-nucleon centre-of-mass energy of 2.76 TeV". In: *JHEP* 1108 (2011), p. 141. DOI: 10.1007/JHEP08(2011)141. arXiv: 1107.4800 [nucl-ex] (cit. on p. 11).

[15] ATLAS Collaboration. "Measurement of the centrality dependence of the charged particle pseudorapidity distribution in lead–lead collisions at with the {ATLAS} detector". In: *Physics Letters B* 710.3 (2012), pp. 363–382. ISSN: 0370-2693. DOI: http://dx.doi.org/10.1016/j.physletb.2012.02.045. URL: http://www.sciencedirect.com/science/article/pii/S0370269312001864 (cit. on p. 11).

[16] STAR Collaboration. "Systematic measurements of identified particle spectra in *pp*, d + Au, and Au + Au collisions at the STAR detector". In: *Phys. Rev. C* 79 (3 Mar. 2009), p. 034909. DOI: 10.1103/PhysRevC.79.034909. URL: http://link.aps.org/doi/10.1103/PhysRevC.79.034909 (cit. on pp. 11–13).

[17] ALICE Collaboration. "Pion, Kaon, and Proton Production in Central Pb-Pb Collisions at $\sqrt{s_{NN}}$=2.76 TeV". In: *Phys. Rev. Lett.* 109 (25 Dec. 2012), p. 252301. DOI: 10.1103/PhysRevLett.109.252301. URL: http://link.aps.org/doi/10.1103/PhysRevLett.109.252301 (cit. on pp. 12, 13).

[18] PHENIX Collaboration. "Identified charged particle spectra and yields in Au + Au collisions at $\sqrt{s_{NN}} = 200$ GeV". In: *Phys. Rev. C* 69 (3 Mar. 2004), p. 034909. DOI: 10.1103/PhysRevC.69.034909. URL: http://link.aps.org/doi/10.1103/PhysRevC.69.034909 (cit. on pp. 12, 13).

[19] Chun Shen et al. "Radial and elliptic flow in Pb + Pb collisions at energies available at the CERN Large Hadron Collider from viscous hydrodynamics". In: *Phys. Rev. C* 84 (4 Oct. 2011), p. 044903. DOI: 10.1103/PhysRevC.84.044903. URL: http://link.aps.org/doi/10.1103/PhysRevC.84.044903 (cit. on pp. 12, 13).

[20] Yu A Karpenko and Yu M Sinyukov. "Femtoscopic scales in central A+A collisions at RHIC and LHC energies in a hydrokinetic model". In: *Journal of Physics G: Nuclear and Particle Physics* 38.12 (2011), p. 124059. URL: http://stacks.iop.org/0954-3899/38/i=12/a=124059 (cit. on pp. 12, 13).

[21] Piotr Bozek. "Hydrodynamic flow from RHIC to LHC". In: *Acta Phys.Polon.* B43 (2012), p. 689. DOI: 10.5506/APhysPolB.43.689. arXiv: 1111.4398 [nucl-th] (cit. on pp. 12, 13).

[22] Maciej Rybczynski, Wojciech Florkowski, and Wojciech Broniowski. "Single-freeze-out model for ultra relativistic heavy-ion collisions at $\sqrt{s_{NN}} = 2.76$ TeV and the LHC proton puzzle". In: *Phys.Rev.* C85 (2012), p. 054907. DOI: 10.1103/PhysRevC.85.054907. arXiv: 1202.5639 [nucl-th] (cit. on p. 12).

[23] S. Voloshin and Y. Zhang. "Flow study in relativistic nuclear collisions by Fourier expansion of Azimuthal particle distributions". In: *Z. Phys.* C70 (1996), pp. 665–672. DOI: 10.1007/s002880050141. arXiv: hep-ph/9407282 (cit. on p. 13).

[24] Ulrich W. Heinz. "Concepts of heavy ion physics". In: (2004). These lecture notes are an expanded version of the lectures I gave a year earlier at the 2002 European School of High-Energy Physics in Pylos (Greece) whose Proceedings were published as a CERN Yellow Report (CERN-2004-001, N. Ellis and R. Fleischer, eds.) The online version of these lecture notes on the ArXiv has most graphs presented in color. PPF-SUBJECT = Experimental, Theoretical, pp. 165–238. arXiv: hep-ph/0407360 [hep-ph] (cit. on p. 14).

[25] STAR Collaboration. "Azimuthal anisotropy in Au+Au collisions at $\sqrt{s_{NN}} = 200$ GeV". In: *Phys. Rev. C* 72 (1 July 2005), p. 014904. DOI: 10.1103/PhysRevC.72.014904. URL: http://link.aps.org/doi/10.1103/PhysRevC.72.014904 (cit. on p. 14).

[26] PHENIX Collaboration. "Elliptic Flow of Identified Hadrons in Au + Au Collisions at $\sqrt{s_{NN}} = 200$ GeV". In: *Phys. Rev. Lett.* 91 (18 Oct. 2003), p. 182301. DOI: 10.1103/PhysRevLett.91.182301. URL: http://link.aps.org/doi/10.1103/PhysRevLett.91.182301 (cit. on p. 14).

[27] You Zhou. "Anisotropic flow of identified particles in Pb–Pb collisions at $\sqrt{s_{NN}} = 2.76$ TeV with the ALICE detector". In: *J.Phys.Conf.Ser.* 509 (2014), p. 012029. DOI: 10.1088/1742-6596/509/1/012029. arXiv: 1309.3237 [nucl-ex] (cit. on pp. 14, 15).

[28] Ulrich Heinz, Chun Shen, and Huichao Song. "The viscosity of quark-gluon plasma at RHIC and the LHC". In: *AIP Conf.Proc.* 1441 (2012), pp. 766–770. DOI: 10.1063/1.3700674. arXiv: 1108.5323 [nucl-th] (cit. on pp. 14, 15).

[29] Xin-Nian Wang, Miklos Gyulassy, and Michael Plümer. "Landau-Pomeranchuk-Migdal effect in QCD and radiative energy loss in a quark-gluon plasma". In: *Phys. Rev. D* 51 (7 Apr. 1995), pp. 3436–3446. DOI: 10.1103/PhysRevD.51.3436. URL: http://link.aps.org/doi/10.1103/PhysRevD.51.3436 (cit. on p. 15).

[30] Betty Abelev et al. "Centrality Dependence of Charged Particle Production at Large Transverse Momentum in Pb–Pb Collisions at $\sqrt{s_{NN}} = 2.76$ TeV". In: *Phys.Lett.* B720 (2013), pp. 52–62. DOI: 10.1016/j.physletb.2013.01.051. arXiv: 1208.2711 [hep-ex] (cit. on pp. 17, 18).

[31] STAR Collaboration. "Transverse-Momentum and Collision-Energy Dependence of High-p_T Hadron Suppression in Au + Au Collisions at Ultrarelativistic Energies". In: *Phys. Rev. Lett.* 91 (17 Oct. 2003), p. 172302. DOI: 10.1103/PhysRevLett.91.172302. URL: http://link.aps.org/doi/10.1103/PhysRevLett.91.172302 (cit. on p. 17).

[32] PHENIX Collaboration. "High-p_T charged hadron suppression in Au + Au collisions at $\sqrt{s_{NN}} = 200$ GeV". In: *Phys. Rev. C* 69 (3 Mar. 2004), p. 034910. DOI: 10.1103/PhysRevC.69.034910. URL: http://link.aps.org/doi/10.1103/PhysRevC.69.034910 (cit. on p. 17).

[33] Serguei Chatrchyan et al. "Study of high-pT charged particle suppression in PbPb compared to pp collisions at $\sqrt{s_{NN}} = 2.76$ TeV". In: *Eur.Phys.J.* C72 (2012), p. 1945. DOI: 10.1140/epjc/s10052-012-1945-x. arXiv: 1202.2554 [nucl-ex] (cit. on pp. 17, 18).

[34] ALICE Collaboration. "The ALICE experiment at the CERN LHC". In: *Journal of Instrumentation* 3.08 (2008), S08002. URL: %7Bhttp://stacks.iop.org/1748-0221/3/i=08/a=S08002%7D (cit. on p. 22).

[35] ALICE Collaboration. *ALICE Offline framework, AliRoot*. URL: http://aliceinfo.cern.ch/Offline (cit. on p. 28).

[36] R. Brun and F. Rademakers. "ROOT: An object oriented data analysis framework". In: *Nucl.Instrum.Meth.* A389 (1997), pp. 81–86. DOI: 10.1016/S0168-9002(97)00048-X (cit. on p. 28).

[37] Rene Brun, Federico Carminati, and Simone Giani. "GEANT Detector Description and Simulation Tool". In: (1994) (cit. on p. 28).

[38] S. Agostinelli et al. "GEANT4: A Simulation toolkit". In: *Nucl.Instrum.Meth.* A506 (2003), pp. 250–303. DOI: 10.1016/S0168-9002(03)01368-8 (cit. on p. 28).

[39] A. Fasso et al. "The FLUKA code: Present applications and future developments". In: *eConf* C0303241 (2003), MOMT004. arXiv: physics/0306162 [physics] (cit. on p. 28).

[40] Torbjorn Sjostrand, Stephen Mrenna, and Peter Z. Skands. "PYTHIA 6.4 Physics and Manual". In: *JHEP* 0605 (2006), p. 026. DOI: 10.1088/1126-6708/2006/05/026. arXiv: hep-ph/0603175 [hep-ph] (cit. on p. 28).

[41] G. Corcella et al. "HERWIG 6: An Event generator for hadron emission reactions with interfering gluons (including supersymmetric processes)". In: *JHEP* 0101 (2001), p. 010. DOI: 10.1088/1126-6708/2001/01/010. arXiv: hep-ph/0011363 [hep-ph] (cit. on p. 28).

[42] Xin-Nian Wang and Miklos Gyulassy. "hijing". In: *Phys. Rev. D* 44 (11 Dec. 1991), pp. 3501–3516. DOI: 10.1103/PhysRevD.44.3501. URL: http://link.aps.org/doi/10.1103/PhysRevD.44.3501 (cit. on p. 29).

[43] Stefan Roesler, Ralph Engel, and Johannes Ranft. "The Monte Carlo event generator DPMJET-III". In: (2000), pp. 1033–1038. arXiv: hep-ph/0012252 [hep-ph] (cit. on p. 29).

[44] P. Saiz et al. "AliEn—ALICE environment on the {GRID}". In: *Nuclear Instruments and Methods in Physics Research Section A: Accelerators, Spectrometers, Detectors and Associated Equipment* 502.2–3 (2003). Proceedings of the {VIII} International Workshop on Advanced Computing and Analysis Techniques in Physics Research, pp. 437–440. ISSN: 0168-9002. DOI: http://dx.doi.org/10.1016/S0168-9002(03)00462-5. URL: http://www.sciencedirect.com/science/article/pii/S0168900203004625 (cit. on pp. 29, 30).

[45] L Musa and K Safarik. *Letter of Intent for the Upgrade of the ALICE Experiment*. Tech. rep. CERN-LHCC-2012-012. LHCC-I-022. Geneva: CERN, Aug. 2012 (cit. on pp. 31, 35).

[46] ALICE Collaboration. *Addendum of the Letter Of Intent for the Upgrade of the ALICE Experiment : The Muon Forward Tracker*. Tech. rep. CERN-LHCC-2013-014. LHCC-I-022-ADD-1. Final submission of the presetn LoI addendum is scheduled for September 7th. Geneva: CERN, Aug. 2013 (cit. on pp. 32, 35).

[47] ALICE Collaboration. *Technical Design Report for the Upgrade of the ALICE Inner Tracking System*. Tech. rep. CERN-LHCC-2013-024. ALICE-TDR-017. Geneva: CERN, Nov. 2013 (cit. on pp. 35, 36, 38, 40).

[48] Alessandro Grelli. "D meson nuclear modification factors in Pb-Pb collisions at $\sqrt{s_{NN}} = 2.76$ TeV with the ALICE detector". In: *Nucl.Phys.* A904-905 (2013), pp. 635c–638c. DOI: 10.1016/j.

nuclphysa.2013.02.096. arXiv: 1210.7332 [hep-ex] (cit. on pp. 38, 40).

[49] L Musa. *Conceptual Design Report for the Upgrade of the ALICE ITS*. Tech. rep. CERN-LHCC-2012-005. LHCC-G-159. Geneva: CERN, Mar. 2012 (cit. on pp. 39, 40).

[50] G. Schneider. *Installation of the central beryllium beam pipe in the alice experiment.* Tech. rep. EDMS: 1113439. Geneva: CERN, 2011 (cit. on p. 41).

[51] L. Rossi et al. *Pixel Detectors: From Fundamentals to Applications*. Particle Acceleration and Detection. Springer, 2006. ISBN: 9783540283331. URL: http://books.google.it/books?id=AKGIXQOm0-EC (cit. on p. 46).

[52] L. Landau. "On the energy loss of fast particles by ionization". In: *J.Phys.(USSR)* 8 (1944), pp. 201–205 (cit. on p. 47).

[53] P.V. Vavilov. "Ionization losses of high-energy heavy particles". In: (Nov. 1957) (cit. on p. 47).

[54] Gerald R. Lynch and Orin I. Dahl. "Approximations to multiple Coulomb scattering". In: *Nuclear Instruments and Methods in Physics Research Section B: Beam Interactions with Materials and Atoms* 58.1 (1991), pp. 6–10. ISSN: 0168-583X. DOI: http://dx.doi.org/10.1016/0168-583X(91)95671-Y. URL: http://www.sciencedirect.com/science/article/pii/0168583X9195671Y (cit. on p. 47).

[55] W.R. Leo. *Techniques for Nuclear and Particle Physics Experiments: A How-to Approach*. Springer, 1994. ISBN: 9780387572802. URL: http://books.google.it/books?id=W7vHQgAACAAJ (cit. on pp. 48, 64).

[56] L. Greiner et al. "A {MAPS} based vertex detector for the {STAR} experiment at {RHIC}". In: *Nuclear Instruments and Methods in Physics Research Section A: Accelerators, Spectrometers, Detectors and Associated Equipment* 650.1 (2011). International Workshop on Semiconductor Pixel Detectors for Particles and Imaging 2010, pp. 68–72. ISSN: 0168-9002. DOI: http://dx.doi.org/10.1016/j.nima.2010.12.006. URL: http://www.sciencedirect.com/science/article/pii/S0168900210027439 (cit. on p. 50).

[57] J.A. Ballin et al. "Monolithic Active Pixel Sensors {MAPS} in a quadruple well technology for nearly 100% fill factor and full CMOS pixels". In: (2008). arXiv: 0807.2920 [physics.ins-det] (cit. on p. 53).

[58] A. Dorokhov et al. "High resistivity {CMOS} pixel sensors and their application to the {STAR} {PXL} detector". In: *Nuclear Instruments and Methods in Physics Research Section A: Accelerators, Spectrometers, Detectors and Associated Equipment* 650.1 (2011). International Workshop on Semiconductor Pixel Detectors for Par-

ticles and Imaging 2010, pp. 174–177. ISSN: 0168-9002. DOI: http://dx.doi.org/10.1016/j.nima.2010.12.112. URL: http://www.sciencedirect.com/science/article/pii/S0168900210028925 (cit. on p. 56).

[59] W. Snoeys et al. "Layout techniques to enhance the radiation tolerance of standard {CMOS} technologies demonstrated on a pixel detector readout chip". In: *Nuclear Instruments and Methods in Physics Research Section A: Accelerators, Spectrometers, Detectors and Associated Equipment* 439.2–3 (2000), pp. 349–360. ISSN: 0168-9002. DOI: http://dx.doi.org/10.1016/S0168-9002(99)00899-2. URL: http://www.sciencedirect.com/science/article/pii/S0168900299008992 (cit. on pp. 59, 69).

[60] S. Siddhanta et al. "The Readout System for the ALICE Zero Degree Calorimeters". In: *Nuclear Science, IEEE Transactions on* 58.4 (Aug. 2011), pp. 1759–1765. ISSN: 0018-9499. DOI: 10.1109/TNS.2011.2159514 (cit. on p. 63).

[61] Lantronix Inc. *XPort Description*. 2013. URL: https://web.archive.org/web/20130827022033/http://www.lantronix.com/device-networking/embedded-device-servers/xport.html (cit. on p. 63).

[62] M.-M. Bé et al. *Table of Radionuclides*. Vol. 3. Monographie BIPM-5. Pavillon de Breteuil, F-92310 Sèvres, France: Bureau International des Poids et Mesures, 2006. ISBN: 92-822-2218-7. URL: http://www.bipm.org/utils/common/pdf/monographieRI/Monographie_BIPM-5_Tables_Vol3.pdf (cit. on p. 64).

[63] M Berger and M Berger. *Stopping-Power and Range Tables for Electrons, Protons, and Helium Ions: Physical Reference Data*. Gaithersburg, MD: NIST, 1999. URL: http://www.nist.gov/pml/data/star/ (cit. on p. 63).

[64] M. J. Berger et al. "XCOM: Photon Cross Sections Database". In: *NIST Standard Reference Database 8 (XGAM)* (2010). URL: http://www.nist.gov/pml/data/xcom/ (cit. on p. 63).

[65] B.G. Lowe. "Measurements of Fano factors in silicon and germanium in the low-energy X-ray region". In: *Nuclear Instruments and Methods in Physics Research Section A: Accelerators, Spectrometers, Detectors and Associated Equipment* 399.2–3 (1997), pp. 354–364. ISSN: 0168-9002. DOI: http://dx.doi.org/10.1016/S0168-9002(97)00965-0. URL: http://www.sciencedirect.com/science/article/pii/S0168900297009650 (cit. on p. 64).

[66] F. Scholze et al. "Determination of the electron–hole pair creation energy for semiconductors from the spectral responsivity of photodiodes". In: *Nuclear Instruments and Methods in Physics Research Section A: Accelerators, Spectrometers, Detectors and Associated Equipment* 439.2–3 (2000), pp. 208–215. ISSN: 0168-9002.

DOI: http://dx.doi.org/10.1016/S0168-9002(99)00937-7. URL: http://www.sciencedirect.com/science/article/pii/S0168900299009377 (cit. on p. 64).

[67] P. La Rocca. Private communication. 2014 (cit. on p. 72).

[68] Wojciech Dulinski et al. "Beam telescope for medium energy particles based on thin, submicron precision MAPS". In: (2003), pp. 995–1002. DOI: 10.1109/NSSMIC.2007.4437182 (cit. on p. 83).

[69] M. Gelin et al. "Intermediate Digital Monolithic Pixel Sensor for the EUDET High Resolution Beam Telescope". In: *Nuclear Science, IEEE Transactions on* 56.3 (June 2009), pp. 1677–1684. ISSN: 0018-9499. DOI: 10.1109/TNS.2009.2017921 (cit. on p. 84).

[70] *Institut Pluridisciplinaire Hubert CURIEN, Public Documentation*. URL: http://www.iphc.cnrs.fr/Public-documentation.html (cit. on p. 85).